Scripta Materialia 202 (2021) 114007

Contents lists available at ScienceDirect

Scripta Materialia

journal homepage: www.elsevier.com/locate/scriptamat

Cu precipitation-mediated formation of reverted austenite during ageing of a 15–5 PH stainless steel

Tao Zhou[a,*], Benjamin Neding[a], Sen Lin[a], Jo-Chi Tseng[b], Peter Hedström[a]

[a] Department of Materials Science and Engineering, KTH Royal Institute of Technology, SE-100 44 Stockholm, Sweden
[b] Deutsches Elektronen-Synchrotron, DESY, D-22603 Hamburg, Germany

ARTICLE INFO

Article history:
Received 18 March 2021
Revised 11 May 2021
Accepted 19 May 2021
Available online 1 June 2021

Keywords:
Austenitic transformation
Precipitation
In situ X-ray diffraction
Atom probe tomography
Computational thermodynamics

ABSTRACT

A Cu precipitation-mediated austenitic transformation during ageing treatment of a 15–5 PH stainless steel is revealed through atom probe tomography, *in situ* synchrotron X-ray diffraction and computational thermodynamics and kinetics. The austenitic transformation is proposed to occur through the pathway: Cu precipitation at the martensite/retained austenite interfaces or at martensite lath boundaries → partitioning of austenite stabilizing elements towards interfaces of the Cu precipitates → reverted austenite formation.

Maraging stainless steels, such as 17–4 PH and 15–5 PH, have wide applications in *e.g.* aerospace and nuclear industry where the combination of strength, toughness, corrosion resistance and weldability is required [1–3]. The properties of maraging stainless steels can be tuned by controlling the microstructural evolution during the final ageing treatment. This microstructural evolution is complex with the occurrence of several interrelated microstructural phenomena such as dislocation annihilation, stress relaxation, lath martensite coarsening, formation of reverted austenite and precipitation of multiple particles (Cu, G phase, Cr-rich phase, Si-rich phase, Nb-rich phase, secondary carbides, *etc.* [4–9]). In the present work we specifically target the correlation between the formation of reverted austenite, Cu precipitation and elemental partitioning that occur during the ageing treatment of a 15–5 PH steel. The seminal work by Couturier et al. [6] reveals several interesting microstructural features of a quenched and aged 15–5 PH steel: i) the microstructure is not fully martensitic after quenching from the solution treatment temperature, and the small amount of austenite present after quenching increases during the subsequent ageing, *i.e.* reverted austenite forms; ii) retained austenite and reverted austenite were distinguished based on the knowledge that the retained austenite maintains the composition of the high-temperature austenite whereas the reverted austenite is enriched with austenite stabilizers (Ni, Mn, C); iii) the identified reverted austenite forms at the martensite/retained austenite interfaces and at martensite lath boundaries; iv) the identified reverted austenite has a high density of Cu precipitates, suggested to indicate the formation of Cu precipitates prior to the formation of reverted austenite. In the present work we add further explanations to the microstructural evolution in 15–5 PH steel during ageing by elaborating on the microstructural transformation pathway discussed in Couturier et al. [6]. We designate this transformation pathway as Cu precipitation-mediated reverted austenite formation. We propose that: firstly, Cu precipitation occurs at the tempered martensite/retained austenite interfaces or at martensite lath boundaries; secondly, Ni and Mn atoms partition towards interfaces of the Cu precipitates, where a core-shell structure is developed; thirdly, the areas enriched with austenite stabilizers (Ni and Mn) transform into reverted austenite. This microstructural transformation sequence is supported by atom probe tomography (APT) analysis, computational thermodynamics and kinetics, and *in situ* synchrotron X-ray diffraction (SXRD) during ageing treatment.

A commercial 15–5 PH alloy, provided by Outokumpu Stainless, with a nominal composition 0.028C–0.60Si–0.69Mn–15.67Cr–4.92Ni–0.42Mo–0.25Nb–3.29Cu–Fe balance (wt%) was investigated. The heat treatment was conducted in a tube furnace with protective argon atmosphere. Solution treatment was performed at 1170 °C for 1 h prior to quenching in brine. Thereafter ageing at 500 °C for 20 h was conducted prior to quenching in brine. The aged sample was analysed by APT. The APT measurements were performed using a local-electrode atom-probe (CAMECA LEAP 4000X-HR) equipped with an energy-compensating reflectron for

* Corresponding author.
E-mail address: taozhou@kth.se (T. Zhou).

https://doi.org/10.1016/j.scriptamat.2021.114007

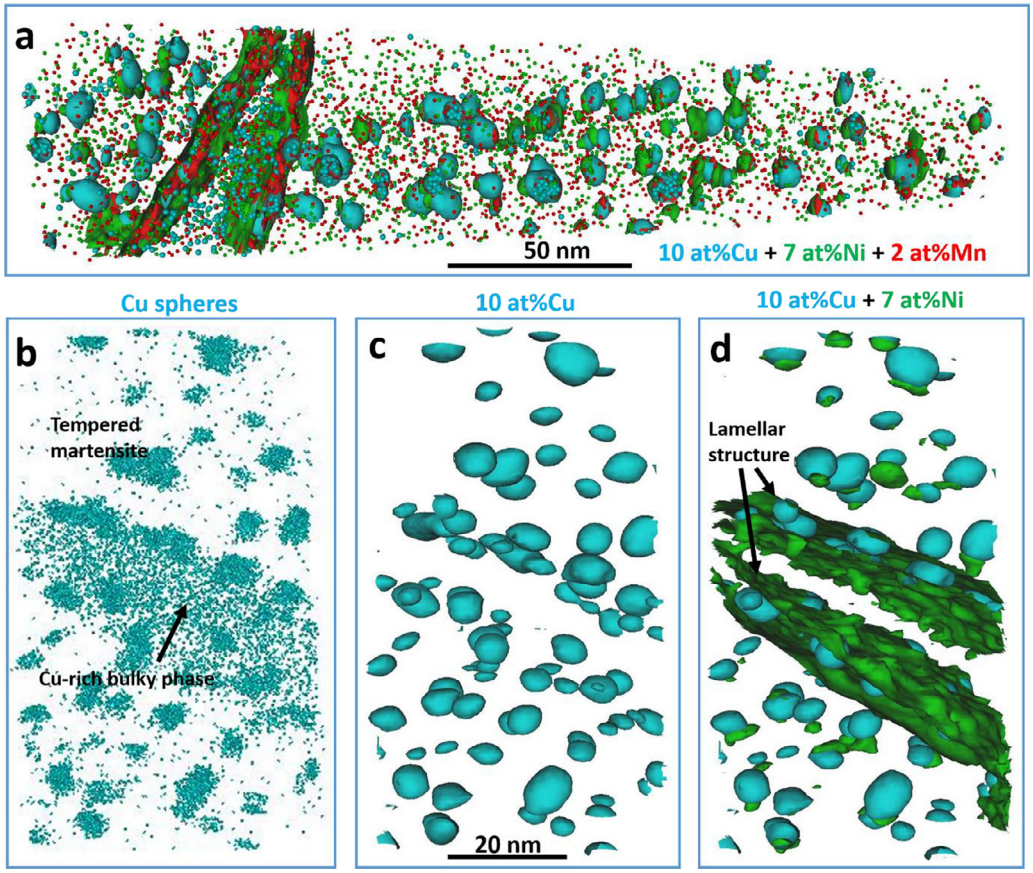

Fig. 1. APT 3D reconstruction of precipitates and elemental distribution in a 20 h aged specimen at 500 °C: (a) the overall view of the measured volume with elemental distribution and isoconcentration analysis of Cu, Ni, and Mn; (b) the distribution of Cu atoms for a selected part of the measured volume; (c) 10 at% Cu isoconcentration analysis, showing the absence of Cu precipitates in the Cu-rich bulky phase; and (d) 10 at% Cu + 7 at% Ni isoconcentration analysis, showing the lamellar structure.

improved mass resolution. The details of sample preparation, measurement parameters, 3D reconstruction and quantitative analysis of Cu precipitates can be found in Ref. [10]. Thermodynamic calculations were performed using the Thermo-Calc software [11] and the TCFE10 database. DICTRA simulation [12] was performed at 500 °C for 6 h, using the thermodynamic database TCFE10 and the diffusion database MOBFE5. A planar two-phase Fe-Cr-Ni-Si-Mn-Mo alloy system was defined with moving boundary consisting of a bcc phase for martensite with the nominal contents of the alloying elements and a cell size of 100 nm divided into 50 grid points with a geometric ratio of 1.05 starting from the zero position, and a fcc nucleus (austenite) attached to the martensite, which should grow during the simulation. *In situ* SXRD experiments during ageing treatment were conducted at the P02.1 beamline at the PETRA III synchrotron source, DESY, Germany [13]. A sample with the dimensions $1 \times 1 \times 15$ mm^3 was measured using a monochromatic X-ray beam with an energy of 59.866 keV (wavelength: 0.20713 Å). The temperature control was imposed with the aid of a Linkam furnace T95 with a precision of 1 °C. The X-ray beam was collimated to 0.4×0.2 mm^2. The sample to detector distance was about 1287 mm, precisely determined by using measurements from a standard CeO_2 powder specimen prior to the analysis of the *in situ* measurements. *In situ* measurements were conducted for a total duration of 6 h ageing at 500 °C. This treatment was performed in three steps, including: heating from RT to 500 °C at a rate of ~ 0.5 °C/s, isothermal holding for 2 h, and cooling from 500 °C to RT at a rate of ~ 0.5 °C/s. This was done on an as-quenched sample which was heat treated in a tube furnace prior to the *in situ* X-ray measurements. 2D diffraction patterns were acquired every 10 s with a Perkin-Elmer EN1621 area detector. The software package Fit2D [14,15] was used to integrate the 2D patterns into 1D patterns. Austenitic peaks 111γ, 200γ and 220γ, and tempered martensitic peaks 110α, 200α and 211α were fitted using pseudo-Voigt function through multi-peak fitting in the software LIPRAS [16]. Integrated peak intensities were thereafter used to evaluate the volume fraction of austenite using the direct comparison method [17–19].

Fig. 1a shows the APT reconstruction of precipitates and atoms in the 20 h *ex situ* aged specimen. Cu precipitates are dispersed in the tempered martensitic matrix. Ni and Mn atoms segregate at the Cu precipitates forming a core-shell structure, as known from previous studies [20]. The first interesting structure in this 3D reconstruction is the two lamellar structures (Fig. 1d), which has a higher number density of Cu precipitates (Fig. 1c) and are enriched with Ni and Mn (Fig. 1a). The other interesting structure here is the bulky area between the two lamellar structures. It has a clearly higher Cu concentration than the tempered martensitic matrix (Fig. 1b). In order to understand what these two specific structures are as well as their formation mechanism, a comparison of the chemical analysis from APT and thermodynamic calculations (see Table 1) is carried out. It is found that the Cu-rich bulky structure has almost the same composition as the nominal composition of the material, suggesting that this structure is austenite retained after quenching from the solution treatment. This result is consistent with previous work [6]. The composition of the tempered martensitic matrix is almost the same as the equilibrium composition of bcc at 500 °C as calculated by Thermo-Calc. The agreement between the thermodynamic calculations and the APT analyses for the retained austenite and the tempered martensitic matrix indi-

Table 1
Comparison of compositions (at%) of phases and structures from APT analysis and thermodynamic calculation.

Phases (method)	Fe	Ni	Mn	Si	Cr	Cu	Nb	Mo	C
Nominal composition of the materials	73.0	4.6	0.69	1.2	16.7	2.9	0.15	0.24	0.13
Cu-rich bulky phase (APT)	74.1	4.0	0.83	1.6	16.7	2.3	0.08	0.23	$1.9E^{-2}$
Tempered martensite (Thermo-Calc)	80.3	3.6	0.34	0.94	14.7	0.055	$3.8E^{-4}$	0.029	$5.7E^{-6}$
Tempered martensite (APT)	79.4	2.2	0.48	1.7	15.8	0.089	0.015	0.18	$7.0E^{-3}$
Austenite (Thermo-Calc)	59.6	23.1	2.91	3.2	9.9	1.3	$9.0E^{-4}$	0.026	$1.8E^{-5}$
Lamellar structure including precipitates (APT)	60.6	11.1	1.78	1.7	16.1	8.1	0.099	0.24	$2.9E^{-2}$
Lamellar structure matrix (APT)	62.9	10.7	1.84	2.0	21.4	0.5	0.21	0.26	$6.3E^{-3}$

Table 2
Comparisons of volume fraction, number density, and mean radius of Cu precipitates in the lamellar structure and tempered martensite from APT analysis.

Phases	Number density (m^{-3})	Volume fraction (%)	Mean radius (nm)
Lamellar structure	(4.05 ± 1.23) E23	6.75 ± 2.05	2.85 ± 1.05
Tempered martensite	(1.56 ± 0.61) E23	2.54 ± 1.07	3.05 ± 1.04

cates the reliability of both the APT analyses and the thermodynamic calculations.

The lamellar structure was postulated as reverted austenite based on its Ni/Mn/C-rich feature in the previous work [6]. However, the chemical composition of the reverted austenite was not discussed in relation to computational thermodynamics results, preventing the establishment of a clear rationale for the formation mechanism of the lamellar structure. We try to elucidate this hereafter by combining experimental and computational analyses. Firstly, the concentration profile analysis of the whole lamellar structure including Cu precipitates (using a thicker cylinder as shown in Fig. 2a) or the lamellar structure matrix (using a thinner cylinder through the matrix of the lamellar structure, which is not shown here), shows that the Ni and Mn concentrations are similar in the two cases, but are lower than the equilibrium composition of austenite calculated by Thermo-Calc (see Table 1). In addition, there is a good agreement in the Fe content (about 60 at%) between the APT analysis and the calculation. These results suggest that the lamellar structure is probably reverted austenite, and has still not reached equilibrium composition. It can also be seen from Table 1 and the concentration profile in Fig. 2a and b that the Si contents in tempered marteniste, retained austenite and the lamellar structure are almost the same, *i.e.* no Si segregation was observed, which reduces the likelihood of the lamellar structure to be G phase ($Ni_{16}Mn_6Si_7$). Secondly, proxigram analysis of all the Cu precipitates in the lamellar structure and in the tempered martensitic matrix (see Fig. 2c and d) shows that the maximum Cu concentration at the core is 71.4 ± 5.1 at% and 80.0 ± 5.1 at% for precipitates in the lamellar structure and tempered martensite, respectively. This suggests that the Cu precipitates in both the lamellar structure and tempered martensitic matrix have still not reached equilibrium composition, since the Cu concentration of fcc Cu precipitates in the austenite at equilibrium should be close to 100 at% [21]. In addition, the volume fraction, number density, and mean radius of Cu precipitates are analysed in both the lamellar structure and the tempered martensite for a quantitative comparison (see Table 2). The results show that the volume fraction and number density of Cu precipitates are higher in the lamellar structure than in the tempered martensite, which may result from the lower nucleation barrier for Cu precipitation at the boundaries. The mean radius of Cu precipitates in the lamellar structure and tempered martensite is similar considering the error margin. Thirdly, the chemical driving force for Cu precipitation in austenite as a function of Ni and Mn contents at the ageing temperature 500 °C is calculated by Thermo-Calc (the composition used for the calculation is 16.7Cr-2.9Cu-1.2Si-xNi-yMn-Fe balance (at%)). The results suggest that the driving force for Cu precipitation in austenite is below $2E^{-11}$ J/mol with variations of Ni (0–12 at%) and Mn (0–2 at%) contents in austenite. Since the Cu precipitates cannot form in the retained austenite during ageing (see Fig. 1), it cannot form in the lamellar structure either considering the significantly low driving force for Cu precipitation. On the other hand, the increase of Ni and Mn contents around the core-shell structure enhances the driving force for reverted austenite formation (see Fig. 3). The formation of a (Ni/Mn-rich) shell structure can also be noticed in Fig. 2c and d, where Ni and Mn have a higher concentration around the precipitate-matrix interface as compared to the concentrations within precipitates and matrix, respectively. These observations lead us to propose the following transformation pathway for the lamellar reverted austenite: Cu precipitation occurs at the interfaces of tempered martensite and retained austenite, followed by the segregations of Ni and Mn towards interfaces of the Cu precipitates facilitated by the formation of Cu core-(Ni/Mn-rich) shell structure and fast diffusion rate at the boundaries. This further leads to the formation of reverted austenite around the core-shell structure promoted by the austenite-stabilising elements Ni and Mn.

We have identified the lamellar structure as reverted austenite already, but to further support these observations *in situ* SXRD was employed to quantitatively study the evolution of austenite during the ageing treatment. Fig. 4 shows the kinetic increments in austenite volume fraction during *in situ* ageing at 500 °C. In other words, the y-axis in Fig. 4 means the increment of austenite volume fraction during 500 °C ageing compared to the first datapoint measured when the sample is heated to 500 °C for each cycle. The first cycle shows a relatively high increment rate at the time range of 0–1.5 h. One possible explanation for this is that the high enrichment of austenite-forming elements mediated by Cu precipitates occurs at the boundaries, which leads to a higher formation rate of reverted austenite at the early stage of ageing. At the final stage of the first cycle (after ~ 1.5 h), the formation rate of reverted austenite is mainly determined by the diffusion rate of austenite-forming elements from the tempered martensitic matrix, thus the formation rate of reverted austenite becomes stable, maintaining the same gradient with that of the second and third cycles. The linear fitting of the data-points of the latter two cycles shows that the volume fraction increment rates (*i.e.* the slope of the lines comprised of the data-points) are (0.038 ± 0.002) vol%/h and (0.037 ± 0.003) vol%/h, respectively. It is noteworthy that the above results indicate that the reverted austenite formed during

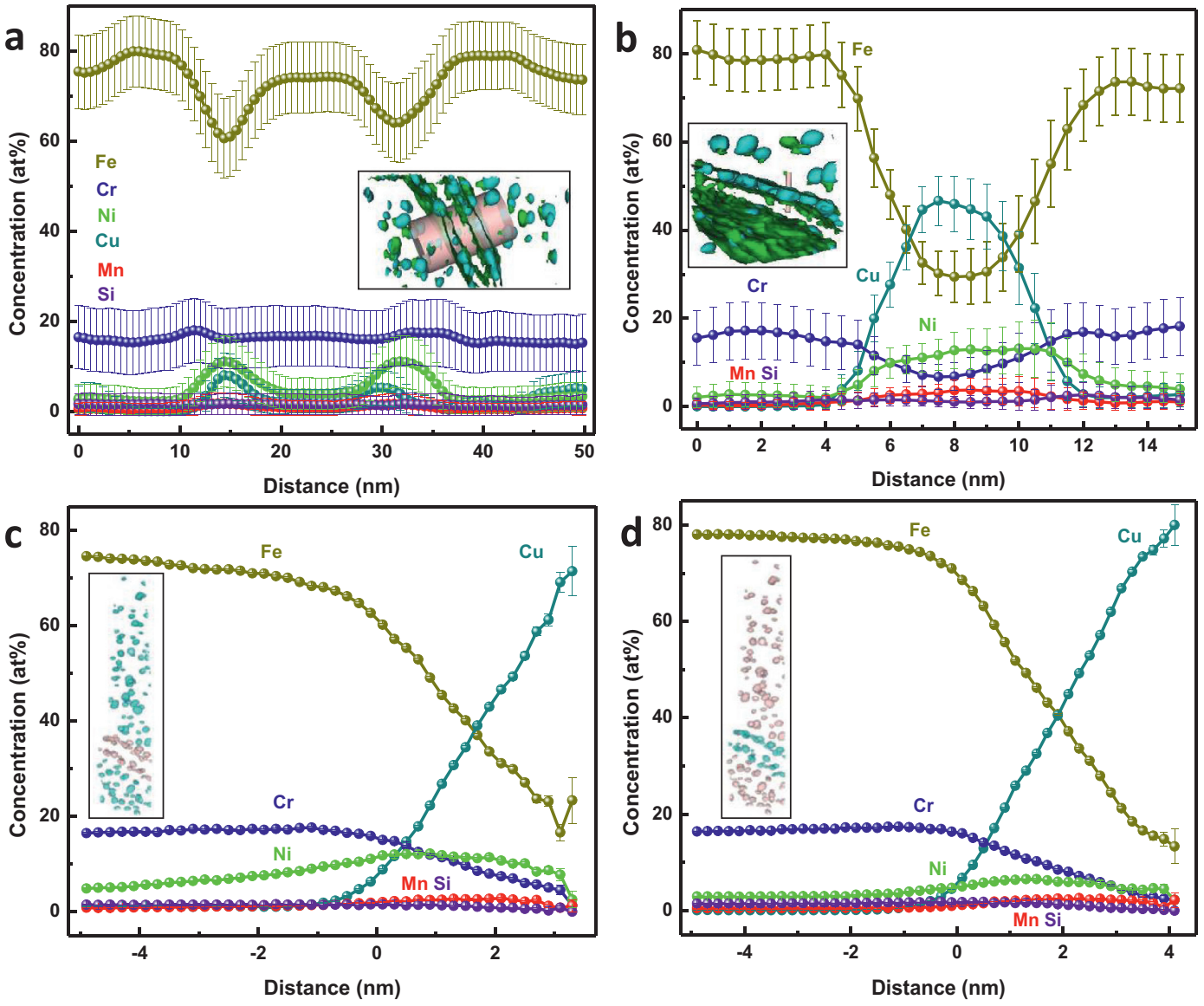

Fig. 2. APT quantitative analysis of elemental partitioning and concentration: (a) concentration profiles of elements through various phases and structures as shown in the inset; (b) concentration profiles of elements through a Cu precipitate within the lamellar structure; (c) proxigram of all Cu precipitates in the lamellar structure; and (d) proxigram of all Cu precipitates in tempered martensite.

ageing is a diffusion-controlled process as the evolution of austenite fraction is highly time-dependant. This is in agreement with the work of Brandl et al. [5] where a diffusion-controlled transformation from martensite to austenite was suggested for 15–5 PH, even though austenitization instead of ageing was investigated there. In order to underpin the SXRD results of reverted austenite formation kinetics, DICTRA simulations of austenite reversion at lath martensite boundaries were performed at 500 °C for 6 h. These simulations show a high increase of the austenite reversion kinetics at the early stage of ageing, which is in agreement with the SXRD results. With the progress of time, the kinetics becomes relatively constant, with a kinetic evolution of (0.018 ± 0.002) vol%/h and (0.014 ± 0.002) vol%/h for the time range 2 to 4 h and 4 to 6 h, respectively. Overall, the DICTRA simulations are in fair agreement with the SXRD results; however, the underestimated kinetics in DICTRA is expected considering mainly the neglected high dislocation density of the martensite that would increase diffusivity.

In summary, the reverted austenite formation kinetics during ageing of a maraging stainless steel 15–5 PH is verified through *in situ* SXRD quantitative analysis and DICTRA simulations. Supported by APT and computational thermodynamics analyses, it is proposed that the mechanism of reverted austenite formation during ageing of maraging stainless steel 15–5 PH, follows the pathway: Cu precipitation at interfaces of tempered martensite and retained austenite due to the lower nucleation barrier at the boundaries → segregations of alloying elements (Ni and Mn) towards the interfaces of Cu precipitates facilitated by the formation of core-shell structure and fast diffusion rate of atoms around boundaries → formation of reverted austenite facilitated by the enrichment of austenite-stabilising elements (Ni and Mn).

This work was performed within the VINN Excellence Centre Hero-m 2i, financed by VINNOVA, the Swedish Government Agency of Innovation Systems, Swedish Industry and KTH. The authors are grateful to PETRA III high-energy synchrotron source, DESY, Germany for providing synchrotron radiation facilities (I-20170197 EC). TZ would like to express his gratitude to the support from Carl Tryggers Foundation (CTS19: 136).

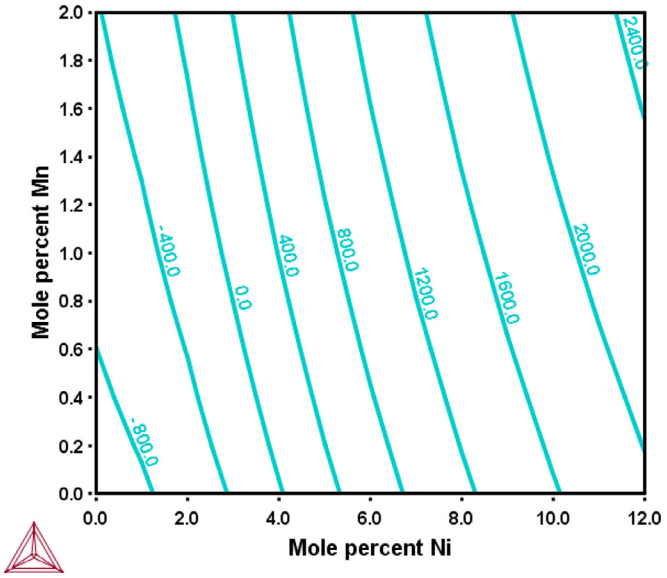

Fig. 3. Computational thermodynamics predictions of chemical driving force (J/mole) for austenite formation in tempered martensite at 500 °C as a function of Ni and Mn contents in tempered martensite. The composition used for the calculation is 14.7Cr-0.055Cu-0.9Si-xNi-yMn-Fe balance (at%).

Declaration of Competing Interest

The authors declare that they have no known competing financial interests or personal relationships that could have appeared to influence the work reported in this paper.

References

[1] T. Zhou, J. Faleskog, R.P. Babu, J. Odqvist, H. Yu, P. Hedström, Mater. Sci. Eng. A 745 (2019) 420–428.
[2] T. Zhou, R.P. Babu, J. Odqvist, H. Yu, P. Hedström, Mater. Des. 143 (2018) 141–149.
[3] J. Wang, H. Zou, C. Li, S.Y. Qiu, B.l. Shen, Mater. Charact. 57 (2006) 274–280.
[4] L. Couturier, F. De Geuser, A. Deschamps. Mater. 9 (2020) 100634.
[5] D. Brandl, M. Lukas, M. Stockinger, S. Ploberger, G. Ressel, Mater. Des. 176 (2019) 107841.
[6] L. Couturier, F. De Geuser, M. Descoins, A. Deschamps, Mater. Des. 107 (2016) 416–425.
[7] Z. Wang, H. Li, Q. Shen, W. Liu, Z. Wang, Acta Mater 156 (2018) 158–171.
[8] G. Yeli, M.A. Auger, K. Wilford, G.D. Smith, P.A. Bagot, M.P. Moody, Acta Mater 125 (2017) 38–49.
[9] J. Wang, H. Zou, C. Li, Y. Peng, S. Qiu, B. Shen, Nucl. Eng. Des. 236 (2006) 2531–2536.
[10] Z. Sheng, M. Bonvalet Rolland, T. Zhou, J. Odqvist, P. Hedström, J. Mater. Sci. 56 (2021) 2650–2671.
[11] J.O. Andersson, T. Helander, L. Höglund, P. Shi, B. Sundman, Calphad 26 (2002) 273–312.
[12] A. Borgenstam, L. Höglund, J. Ågren, A. Engström, J. Phase Equilibria 21 (2000) 269.
[13] A.C. Dippel, H.P. Liermann, J.T. Delitz, P. Walter, H. Schulte-Schrepping, O.H. Seeck, H. Franz, J. Synchrotron Radiat. 22 (2015) 675–687.
[14] A. Hammersley, S. Svensson, M. Hanfland, A. Fitch, D. Hausermann, Int. J. High Press. Res. 14 (1996) 235–248.
[15] A. Hammersley, S. Svensson, A. Thompson, Nucl. Instru. Methods in Phys. Res. A 346 (1994) 312–321.
[16] G. Esteves, K. Ramos, C.M. Fancher, J.L. Jones, LIPRAS: Line-profile analysis Software, 2017, doi:10.13140/RG.2.2.29970.25282/3.
[17] Y. Tian, S. Lin, J.P. Ko, U. Lienert, A. Borgenstam, P. Hedström, Mater. Sci. Eng. A 734 (2018) 281–290.
[18] A.K. De, D.C. Murdock, M.C. Mataya, J.G. Speer, D.K. Matlock, Scripta Mater. 50 (2004) 1445–1449.
[19] S. Lin, U. Borggren, A. Stark, A. Borgenstam, W. Mu, P. Hedström, Metall. Mater. Trans. A 52 (2021) 1812–1825.
[20] Y.R. Wen, A. Hirata, Z.W. Zhang, T. Fujita, C.T. Liu, J.H. Jiang, M.W. Chen, Acta Mater. 61 (2013) 2133–2147.
[21] T. Xi, M.B. Shahzad, D. Xu, J. Zhao, C. Yang, M. Qi, K. Yang, Mater. Sci. Eng., A 675 (2016) 243–252.

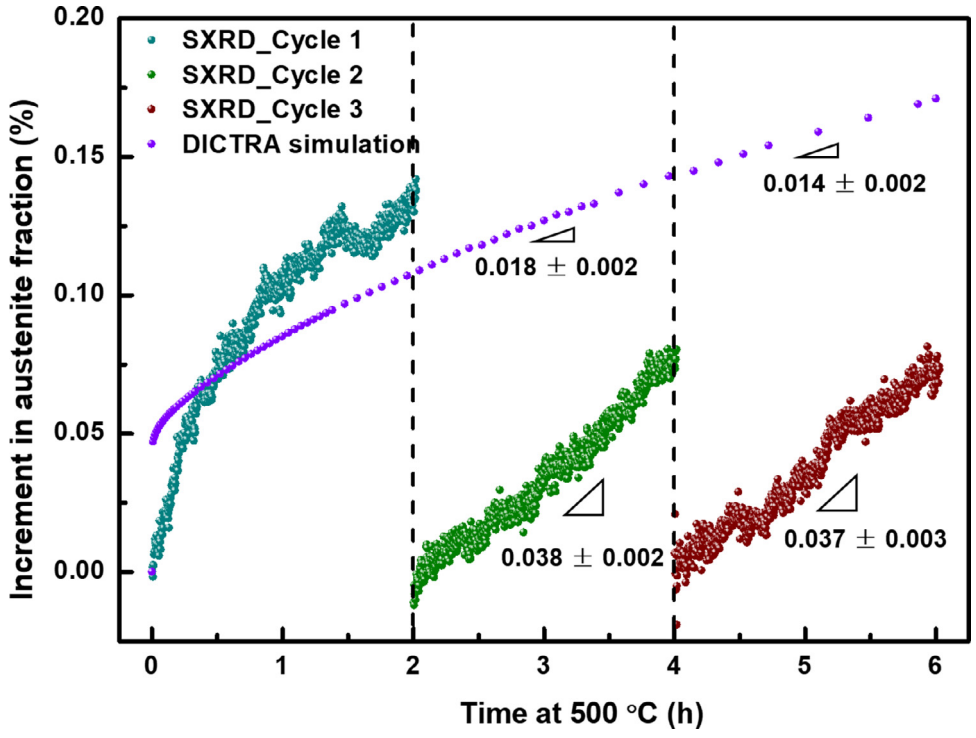

Fig. 4. Comparative analysis of reverted austenite formation kinetics during 500 °C ageing through *in situ* synchrotron X-ray diffraction (SXRD) and DICTRA simulations.